

Article

Research of Gate-Tunable Phase Modulation Metasurfaces Based on Epsilon-Near-Zero Property of Indium-Tin-Oxide

Xin Li ¹, Qiufan Cheng ², Shiliang Guo ^{2,*}  and Zhiquan Li ²

¹ School of Mathematics & Information Technology, Hebei Normal University of Science & Technology, Qinhuangdao 066004, China; lx3671@hevtc.edu.cn

² School of Electrical Engineering, Yanshan University, Qinhuangdao 066004, China; cqf404stu@mail.ysu.edu.cn (Q.C.); lzq54@ysu.edu.cn (Z.L.)

* Correspondence: guosl0112@ysu.edu.cn

Abstract: In this paper, we proposed a reflection phase electrically tunable metasurface composed of an Au/Al₂O₃/ITO/Au grating structure. This antenna array can achieve a broad phase shift continuously and smoothly from 0° to 320° with a 5.85 V applied voltage bias. Tunability arises from field-effect modulation of the carrier concentrations or accumulation layer at the Al₂O₃/ITO interface, which excites electric and magnetic resonances in the epsilon-near-zero region. To make the reflected phase tuning range as wide as possible, some of the intensity of the reflected light is lost due to the excited surface plasmon effect. Simulation results show that the effect of optimal phase modulation can be realized at a wavelength range of 1550 nm by modulating the carrier concentration in our work. Additionally, we utilized an identical 13-unit array metasurface to demonstrate its application to the beam steering function. This active optical metasurface can enable a new realm of applications in ultrathin integrated photonic circuits.

Keywords: phase modulation; field-effect modulation; indium-tin-oxide; epsilon-near-zero materials; surface plasmons



Citation: Li, X.; Cheng, Q.; Guo, S.; Li, Z. Research of Gate-Tunable Phase Modulation Metasurfaces Based on Epsilon-Near-Zero Property of Indium-Tin-Oxide. *Photonics* **2022**, *9*, 323. <https://doi.org/10.3390/photonics9050323>

Received: 8 April 2022

Accepted: 6 May 2022

Published: 9 May 2022

Publisher's Note: MDPI stays neutral with regard to jurisdictional claims in published maps and institutional affiliations.



Copyright: © 2022 by the authors. Licensee MDPI, Basel, Switzerland. This article is an open access article distributed under the terms and conditions of the Creative Commons Attribution (CC BY) license (<https://creativecommons.org/licenses/by/4.0/>).

1. Introduction

With the advancement of ultra-compact optical devices, there is an urgent demand for new structures that can realize the control of the phase and amplitude of the light dynamically [1–8]. Photonics based on 2-dimensional nanostructures, such as metasurfaces, can potentially provide a feasible solution for this specific challenge [9–12]. Metasurfaces are composed of periodic geometry arrays of subwavelength elements such that each element can impose a phase shift and amplitude change on the transmitted, reflected, and scattered light [13–16]. Additionally, there are three essential functions of metasurfaces: beam steering [17], focusing of light [18], and polarization conversion [19]. For example, Liu et al. summarized micromachined tunable metamaterials with mechanical actuation based on mechanical reconfiguration, which has required mechanical movement in recent years [20]. However, this method depends on processing conditions, and the modulation process is not flexible. To respond to the requirement of dynamic tunability, our work is based on optically tunable reflective metasurfaces that have a more comprehensive application prospect than passive metasurfaces [21,22].

The material of choice for the active metasurfaces needs to be quickly and controllably integrated into nanophotonic structures, and if possible, the selected material should be CMOS-compatible, thus allowing integration with on-chip platforms. In a vast regime of wavebands, transparent conductive oxides (TCOs) have been demonstrated as an ideal material that meets the requirements for many reasons, such as the low resistivity, controllable electro-optical property, and the epsilon-near-zero (ENZ) property [23–27]. Indium Tin Oxide (ITO) belongs to this class of material, which is an n-type semiconductor material formed by doping In₂O₃ with Sn in a specific proportion. The advantages of using ITO as an

active material in metasurfaces are manifolds: ITO films can modulate the optical refractive index in a plasmonic cavity configuration and show strong electro-optic solid effects in epsilon-near-zero (ENZ) behavior due to the carrier concentration can be changed in the range of 10^{20} – 10^{21} cm^{-3} [28–30]. To date, industrial advancements, such as magnetron sputtering systems, reactive evaporation, and electrochemical diffusion processes, have made a high yield and reliable process possible, contributing to the wide application of ITO [31,32].

Among the various physical mechanisms for regulating the complex refractive index of materials to achieve phase shifts, field-effect modulation is chosen to offer continuous tunability, shorter response time, and a relatively wide tuning range. It can also provide an amply significant carrier density change in doped semiconductors or conducting oxide, leading to a variable complex refractive index in the charge depletion or accumulation regions [33–35]. Based on the formation principle of charge depletion regions in doped semiconductors, field-effect modulation is a distinctly mature approach in the semiconductor process and is compatible with CMOS [36,37]. For example, Sherrott et al. demonstrated a 237-degree phase modulation range at an operating wavelength of 8.50 μm by using a gate-tunable graphene-gold resonator structure in 2017 [38]. Huang et al. demonstrated an active metasurface realizing the dynamic control of both amplitude and phase [39]. A phase shift of about 225 degrees can be observed at a wavelength around 1550 nm by applying a voltage of 4.6 V in their work. Inspired by these studies, the phase modulation range and the incident wavelength are optimized under a smaller voltage in our work.

In this paper, a dynamically tunable metasurface with a metal–medium–metal grating structure is proposed. We chose ITO as the active material to reach an expansive phase change due to the Fabry–Perot resonance and zero-crossing effect of the permittivity of the ITO accumulation layer. In addition, we simulate a dynamical beam steering device implemented with 30° , 20° , and 10° modulation functions. This optical array will find potential applications in the focusing lens, beam steering device, and polarimeters.

2. Theoretical Models and Design Considerations

A schematic representation of the proposed metasurface structure is shown in Figure 1. We designed tunable metasurfaces composed of an Au back-reflector, on top of which an ITO layer is deposited. This layer is followed by the deposition of a dielectric spacer Al_2O_3 layer and Au nanoantennas. In designing the metasurface element, the physical parameters for the ITO layers should be obtained [40,41]. In our calculations, we assume that the carrier concentration of the active material is $N_0 = 3.2 \times 10^{20}$ cm^{-3} .

When no external bias is applied, the real part permittivity of the ITO layer is positive at a wavelength of 1550 nm. Once under bias, a charge accumulation layer is formed in the ITO, reaching the epsilon-near-zero (ENZ) region with the voltage increasing, which results in a considerable electric field enhancement occurring in the accumulation layer for near-infrared wavelengths. The permittivity dispersion of generic TCO can be described by the Drude model:

$$\varepsilon = \varepsilon_\infty - \frac{\omega_p^2}{\omega^2 + i\omega\gamma} \tag{1}$$

$$\omega_p^2 = \frac{N_0 e_c^2}{\varepsilon_0 m_t} \tag{2}$$

where $\varepsilon_\infty = 3.95$ is the high-frequency permittivity [42]; $\gamma = 180$ THz is the collision frequency; ω_p is the plasma frequency, and ω is the angular frequency of incident light. ε_0 is the vacuum permittivity; $m_t = 0.35 \times m_0$ is the effective mass of electrons in ITO; m_0 is the electron rest mass [43]; e_c is the electron charge, and the initial electron concentration N_0 is set to be 3.2×10^{20} cm^{-3} . Based on Formula (2), the plasma frequency is found to be 1.84×10^{14} $\text{rad}\cdot\text{s}^{-1}$.

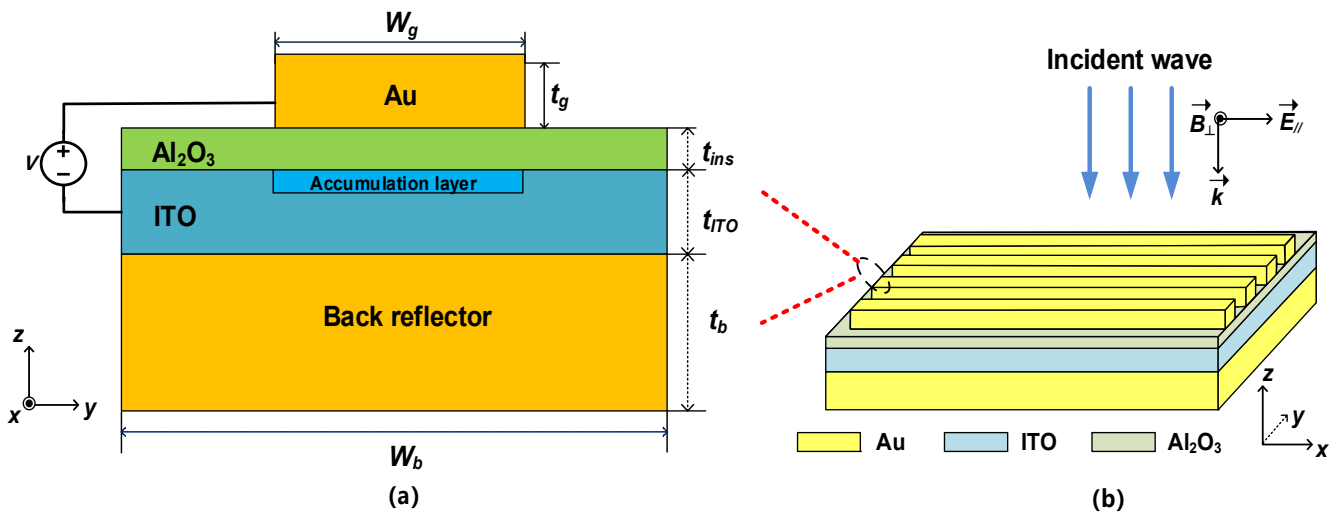


Figure 1. (a) Sectional view of the unit cell of the gate-tunable metasurface composed of an Au back reflector and an ITO layer followed by a gate dielectric on top of which Au antennas are located. The thicknesses of the antenna array, the insulator spacer, the ITO layer, and the back reflector are $t_g = 30$ nm, $t_{ins} = 5$ nm, $t_{ITO} = 20$ nm, and $t_b = 100$ nm, respectively. The antenna dimensions $W_b = 400$ nm, and the electrode width is $W_g = 230$ nm. A voltage bias is applied between the ITO layer and the top antennas. The applied voltage biases result in forming an accumulation/depletion region in the ITO layer at the top, and the TM wave is incident perpendicular to the direction of the metasurface. (b) Schematic of the metasurface. The period of the metasurface is 400 nm.

Another parameter that determines performance is the choice of the plasmonic metal. The relative permittivity of Au is 1.59 [44,45], and our work function of Au is 5.1 eV, which is higher than that of ITO (4.4 eV) when the carrier concentration $N_0 = 3.2 \times 10^{20} \text{ cm}^{-3}$. In addition, selecting Au as a metal electrode in our metasurfaces ensures that the phase change is stable and continuous. The other is the choice of gate dielectric material. Alumina (Al_2O_3) exhibits high DC permittivity and almost perfect interfacial properties with Si-based substrates. It is often employed in field-effect transistor fields as high dielectric constant gate dielectric materials and has a high breakdown field of up to 10 MV/cm. The average thickness t_{acc} of the accumulation layer related to the carriers injected into the ITO layer in a standard metal–insulator–semiconductor structure [46] is given by:

$$t_{acc} = \frac{\pi}{\sqrt{2}} \sqrt{\frac{k_B T \epsilon_0 \epsilon_c}{N_0 e_c^2}} \quad (3)$$

where $k_B = 1.38 \times 10^{-23} \text{ J/K}$ is the Boltzmann constant; $T = 300 \text{ K}$ is the Kelvin temperature; $e_c = 1.6 \times 10^{-19} \text{ C}$ is the electron charge; ϵ_0 is the free space permittivity, and $\epsilon_c = 9.3$ is the relative static permittivity of ITO [47]. Due to the aforementioned $N_0 = 3.2 \times 10^{20} \text{ cm}^{-3}$, the thickness of the accumulation layer is found to be $t_{acc} = 0.7 \text{ nm}$. Then, we can find the carrier concentration N_{acc} in the accumulation layer. Assuming a uniform carrier distribution in the accumulation layer [48], the injected carrier concentration can be calculated as:

$$N_{acc} = \frac{V_g \epsilon_0 \epsilon_{ins}}{e_c \times t_{acc} \times t_{ins}} \quad (4)$$

where $t_{ins} = 5 \text{ nm}$ is the thickness of the insulator spacer, $\epsilon_{ins} = 9$ is the relative permittivity of Al_2O_3 [49], and V_g is the applied voltage.

Based on the above analysis, we can perform optical measurements to illustrate the phase change of incident light with the applied voltage. All the simulations were performed using the numerical simulation software COMSOL Multiphysics based on the finite element method (FEM).

3. Results and Discussion

The metal-insulator-semiconductor field-effect structure was utilized to observe the ENZ region and injected electron density in the ITO accumulation layer. We simulated reflectance and phase modulation of the periodical antenna structure under normal incidence illumination with transverse magnetic (TM) polarization (H-field along with the stripes) based on Figure 1. Electromagnetic waves and frequency domain modules were utilized in our simulation, and the boundary condition was set to a periodic boundary condition. For the ITO layer, we used extremely refined mesh division and free triangular mesh for other areas. Figure 2a,b show the distribution of electromagnetic fields at different applied voltages for a fixed wavelength (1550 nm). The metal grating excites surface plasmon resonance, causing the electric field to converge on the ITO layer, and then changing the dielectric constant of ITO at this time can make the phase changes. At 0 V, symmetrical electric fields between the Au antenna and Au backplane can be observed due to ITO optically behaving as a dielectric ($\epsilon > 0$). In the case of an applied voltage of 2.6 V, the ENZ condition takes up the accumulation layer at the interface of the ITO and Al_2O_3 , and the enhancement of the z-component of the electric field in the accumulation layer is magnified in Figure 2c. As one can see, the real part of the active layer's permittivity (ϵ_{acc}) is 2.093, and the carrier concentration is $3.2 \times 10^{20} \text{ cm}^{-3}$ at no bias for the incident wavelength $\lambda = 1550 \text{ nm}$ in Figure 2d. Based on the carrier concentration model in ITO materials [50,51], it shows that the concentration of carriers within the active layer could rise to $1.1 \times 10^{21} \text{ cm}^{-3}$ with the increasing gate bias, which leads to the permittivity of the accumulation layer changing from a positive one to a negative one. For applied bias values larger than 3.0 V, the permittivity of the accumulation layer is negative, similar to metal. In the case of an applied bias around 2.6 V, ϵ_{acc} is close to zero ($\epsilon_{acc} = 0.041 - 0.58i$), which stimulates the resonance of the local surface plasma, resulting in a steep change of phase shift. This is in line with our expectations of achieving the ENZ region. Figure 2e shows the reflectance and phase shift spectra as a function of the applied voltage. The dotted lines indicate the ENZ region in the accumulation layer at the $\text{Al}_2\text{O}_3/\text{ITO}$ interface. With the gate bias increasing, the magnetic dipole plasmon resonance couples to the ENZ region in the ITO accumulation layer can induce a significant phase shift in reflection [52]. According to this feature, we can study the phase change that conforms to the present description.

As shown in Figure 3a, the designed element phase tuning range (the blue line) is more significant than 300° at $\lambda = 1550 \text{ nm}$, which is obviously better than the phase modulation of the other wavelengths. At 2.65 V bias, the accumulation layer preliminarily reaches the ENZ region, leading to a phase shift of 247° . Based on Formula (5), the phase change is related to the applied voltage [53]. In the ENZ region, the electric field energy is highly confined inside the ITO thin film and fully interacts with the ITO layer. The locally concentrated electric field is very sensitive to changes in the surrounding electromagnetic environment parameters. Therefore, when doping ITO through the bias electrode due to the change in the ITO film's conductivity, the light scattering phase will change sharply, resulting in electrical modulation of the phase. Figure 3b shows the variation between the reflectance of the metasurface and the applied voltage at different wavelengths. With the ENZ condition holding, the plasmonic resonance enhancement is generated in the active layer, leading to the minimum reflectance of 5.9% at 3.35 V shown in Figure 3b. Because critical coupling occurs at the $\text{Al}_2\text{O}_3/\text{ITO}$ interface, the incident wave is absorbed, and the stronger the absorption, the more severe the phase mutation, i.e., the phase change is the most obvious when the amplitude is the lowest.

$$\phi(V) = \frac{2\pi\Delta nL}{\lambda} \quad (5)$$

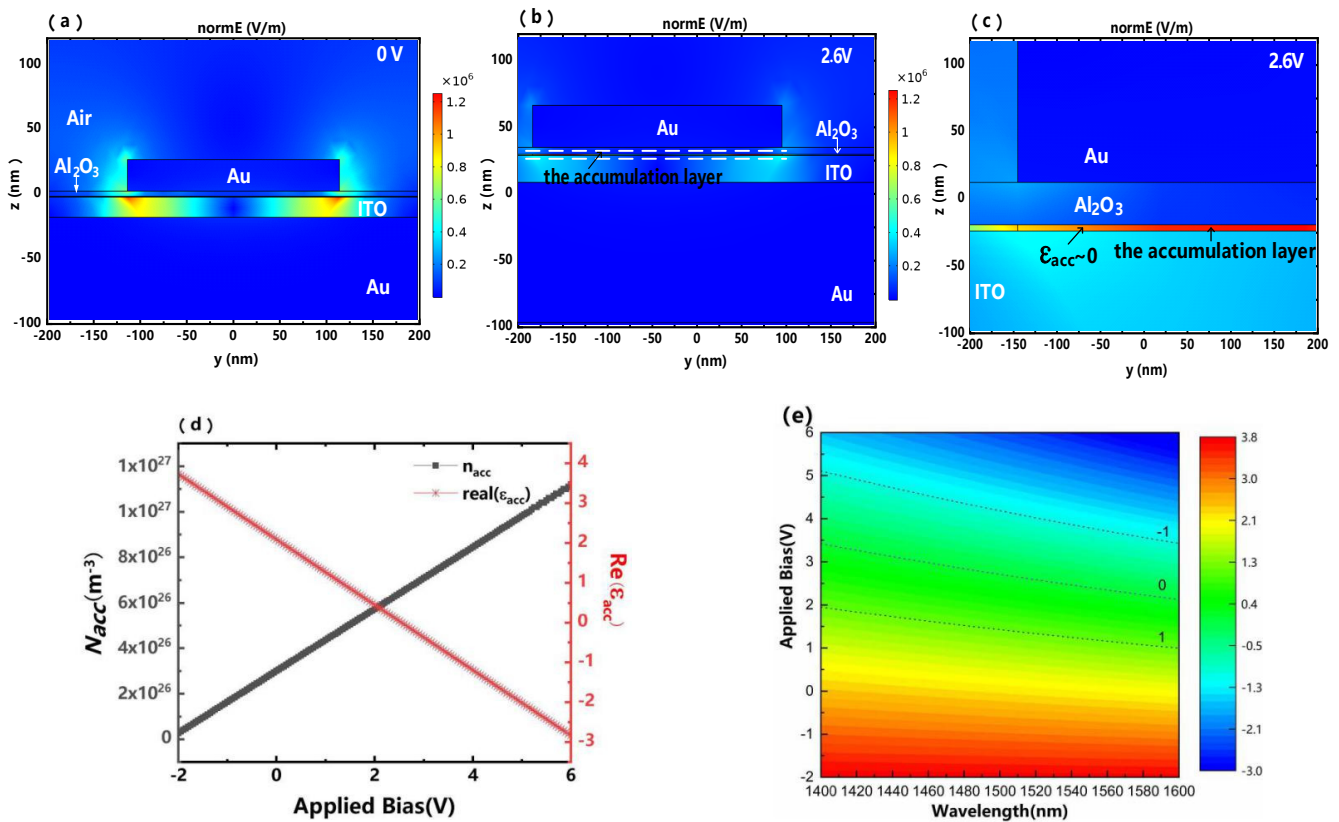


Figure 2. (a,b) is the spatial distribution of the z component of the electric field E_z for applied biases of 0 V and 2.6 V, and (c) is the magnified accumulation region near the Al_2O_3 /ITO interface of 2.6 V applied bias at the wavelength of 1550 nm. The legend represents the magnitude of the electromagnetic field. Simulated (d) is the carrier concentration, and the permittivity of the ITO accumulation layer varies due to gating applied voltage at $\lambda = 1550$ nm. The black line shows carrier concentration variation, and the red line represents different permittivity from -2.8 to 3.7 at the Al_2O_3 /ITO interface. Simulated (e) is the real part of the permittivity spectrum at different bias voltages and wavelengths. The legend represents the value of the dielectric constant at different wavelengths.

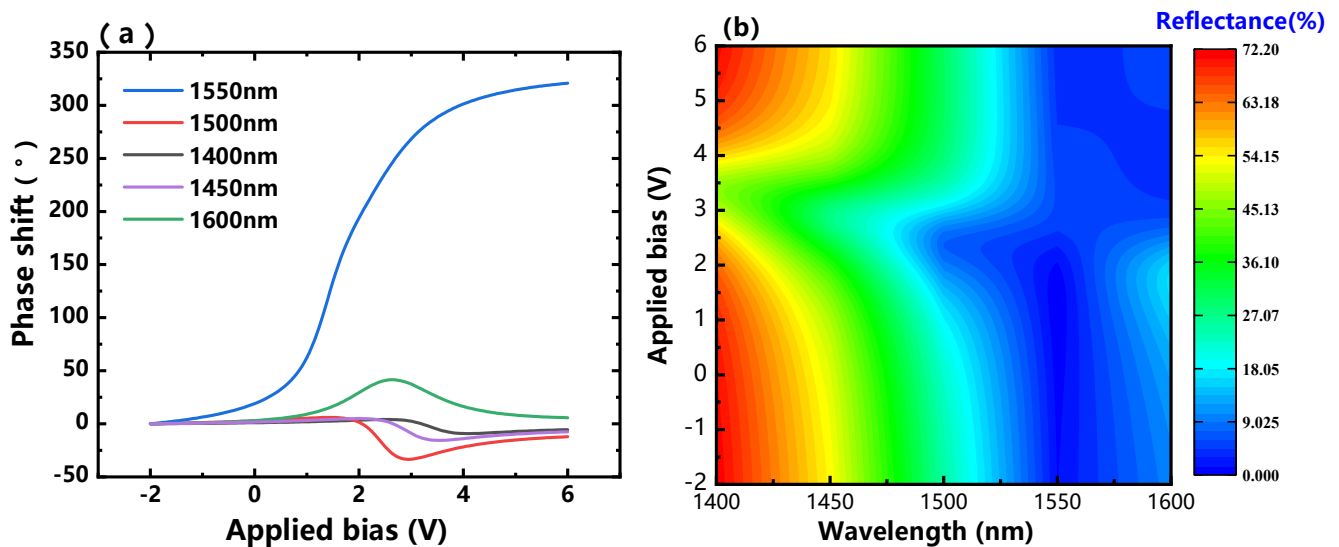


Figure 3. (a) Phase modulation as a function of applied bias for different wavelengths, from 1400 nm to 1600 nm. (b) Simulated reflectance as a function of the applied bias voltage at different wavelengths.

Where Δn is the change in the refractive index of the material caused by the voltage, L is the waveguide length, and ϕ is the phase change. In this case, the reflectance of field-effect modulation is observed at different biases from -2 V to 6 V, which can be understood from the continuity of the normal component of the electric displacement at the field-effect modulation interface. In modern electronic communication, the integration of electronic scales usually requires a nanoscale, and the reduction of device size also requires further energy consumption reduction [52,53]. The designed antenna arrays realized smooth and extensive phase regulation over 300° at near-infrared wavelengths under a smaller voltage condition. Therefore, voltage reduction in our structure is of great significance for future device design.

As demonstrated in the above results, a significant phase change can be achieved in this gated active reflective metasurface. We further employed 13 independent unit cells to illustrate the function of beam steering. These tunable beam steering components have an identical antenna structure of Au/Al₂O₃/ITO/Au planar layers with a periodicity of 400 nm operating at a wavelength of 1550 nm. Thus, the 13-element metasurface operating over the 1550 nm band has a length of $10 \mu\text{m}$. The array surrounded by air is at the bottom of the simulation region, and the boundary condition is set to the scattering boundary condition. The incident wave propagates vertically from the z -direction, and the electromagnetic beam shown in Figure 4 is reflected by the entire antenna structure. The maximum delay required to steer the antenna over an angle θ is given by [54]:

$$\theta = \arcsin \frac{\varphi_n}{nk_r d} \tag{6}$$

where θ is the deflection angle of the reflected beam, $k_r = \omega/c$ represents the relationship between the phase of the incident wave and the distance, n is the element number, d is the spacing of adjacent array elements, and φ_n is the degrees of the adjacent unit's phase shift. We define a positive scan angle when the antenna looks to the left of the boresight. For our present scenario (where $n = 13$ and $\theta = 10$ deg), the maximum delays required for the angle $+10$ deg with respect to elements $n = 0, 1, 2, \dots$ are $0, 16.1^\circ, 31.8^\circ, \dots$. The simulation results are consistent with our analysis above, which demonstrates the function of beam steering successfully, i.e., each element can satisfy the condition for a fixed phase shift when the incident wave frequency is fixed. The direction of the reflected beam toward $30^\circ, 20^\circ$, and 10° has shown in Figure 4. This shows that the beam deflection of $30^\circ, 20^\circ$, and 10° corresponds to a single element phase difference of $46.5^\circ, 31.8^\circ$, and 16.1° , respectively. This efficient electronically tunable beam steering system will have potential value in the development of ultrathin on-chip applications and sensing devices.

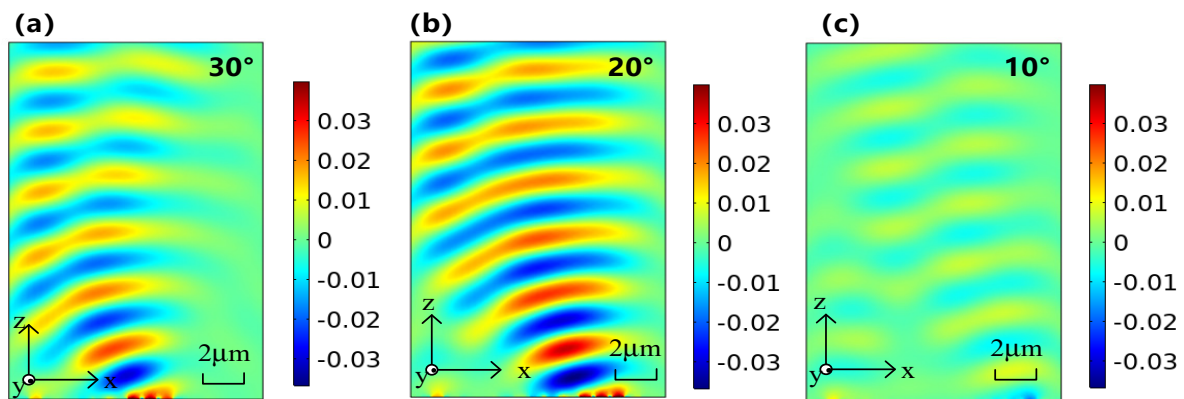


Figure 4. The simulated distributions of the electric field for tunable antennas capable of dynamical angular beam steering toward (a) 30° , (b) 20° , and (c) 10° , respectively. The scale bar is shown in the subfigure. 1 cm on the picture represents the actual distance of $2 \mu\text{m}$. The legend represents the magnitude of the electromagnetic field. The polarization direction of the electric field is the z -direction.

4. Conclusions

In summary, gate-tunable metasurfaces based on Indium-Tin-Oxide were studied in our work. The simulated phase shift can reach 247 degrees by applying a 2.65 V gate bias at a wavelength of 1550 nm, whose maximum phase shift can reach 320 degrees at 5.85 V. This continuous and smooth phase modulation is more than 20 degrees greater than other mid-IR metasurface systems [38,39], which only need a smaller applied voltage. In addition, beam steering with different angles was demonstrated by controlling the phase shift of 13 unit cells, i.e., the phase shift of the adjacent unit moves by 16.1 degrees, and the reflected beam deflects by 10 degrees. This strong light–matter interaction can be explained by the critical coupling of incident waves to the metasurface. The incident light excites eigenmodes through radiative coupling, and the energy is converted into resistive losses under critical coupling conditions so that the reflections are sufficiently suppressed. Phase modulation is a transition state that occurs in under-damped and over-damped oscillations, which means that this transition inevitably passes through a critical coupling region. Therefore, a wide range of phase modulation will be strongly coupled with absorption strength, i.e., with the range of phase tunability increasing, the absorption intensity will also increase, and the phase tunability comes at the expense of energy loss. Due to the critical coupling condition of perfect absorption during the phase change process, in the part with the most severe phase change, the corresponding light absorption is the strongest, and the reflection amplitude is the smallest, at only about 1%. Such a two-dimensional array could enable guidance on devices, such as dynamic holograms, ultrathin lenses, nanoscale light modulators, and polarimeters.

Author Contributions: Q.C. and X.L. contributed to the conception of the study; Q.C. and S.G. contributed to the analysis and manuscript preparation; Q.C. and Z.L. performed the data analyses and wrote the paper. All authors have read and agreed to the published version of the manuscript.

Funding: This work was supported in part by the Natural Science Foundation of Hebei Province grant (No: F2017203316) in China, the Science and Technology Program of Hebei (No: 206Z1703G) in China, the Science and Technology Project of Hebei Education Department (No: ZD2022087) in China, and the Fundamental Research Funds for Provincial Universities (No:2021JK03) in China.

Institutional Review Board Statement: Not applicable.

Informed Consent Statement: Not applicable.

Data Availability Statement: Not applicable.

Conflicts of Interest: The authors declare no conflict of interest.

References

1. Ahmadvand, A.; Gerislioglu, B.; Ramezani, Z. Gated Graphene Island-Enabled Tunable Charge Transfer Plasmon Terahertz Metamodulator. *Nanoscale* **2019**, *11*, 8091–8095. [[CrossRef](#)]
2. Cheng, J.; Fan, F.; Chang, S. Recent Progress on Graphene-Functionalized Metasurfaces for Tunable Phase and Polarization Control. *Nanomaterials* **2019**, *9*, 398. [[CrossRef](#)] [[PubMed](#)]
3. Liu, Z.; Feng, W.; Long, Y.; Guo, S.; Liang, H.; Qiu, Z.; Fu, X.; Li, J. A Metasurface Beam Combiner Based on the Control of Angular Response. *Photonics* **2021**, *8*, 489. [[CrossRef](#)]
4. Zhou, C.; Zhen, M.; Lu, P.; Teng, S. Compound Vector Light Generator Based on a Metasurface. *Photonics* **2021**, *8*, 243. [[CrossRef](#)]
5. Kildishev, A.V.; Boltasseva, A.; Shalaev, V.M. Planar Photonics with Metasurfaces. *Science* **2013**, *339*, 1289. [[CrossRef](#)] [[PubMed](#)]
6. Hsiao, H.; Chu, C.H.; Tsai, D.P. Fundamentals and Applications of Metasurfaces. *Small Methods* **2017**, *1*, 1600064. [[CrossRef](#)]
7. Luo, X.; Pu, M.; Guo, Y.; Li, X.; Ma, X. Electromagnetic Architectures: Structures, Properties, Functions and Their Intrinsic Relationships in Subwavelength Optics and Electromagnetics. *Adv. Photonics Res.* **2021**, *2*, 2100023. [[CrossRef](#)]
8. Yang, X.; Hu, C.; Deng, H.; Rosenmann, D.; Czaplowski, D.A.; Gao, J. Experimental Demonstration of Near-Infrared Epsilon-near-Zero Multilayer Metamaterial Slabs. *Opt. Express* **2013**, *21*, 23631–23639. [[CrossRef](#)]
9. Pang, K.; Alam, M.Z.; Zhou, Y.; Liu, C.; Reshef, O.; Manukyan, K.; Voegtle, M.; Pennathur, A.; Tseng, C.; Su, X.; et al. Adiabatic Frequency Conversion Using a Time-Varying Epsilon-Near-Zero Metasurface. *Nano Lett.* **2021**, *21*, 5907–5913. [[CrossRef](#)]
10. Genevet, P.; Capasso, F. Holographic optical metasurfaces: A review of current progress. *Rep. Prog. Phys.* **2015**, *78*, 024401. [[CrossRef](#)]

11. Genevet, P.; Capasso, F.; Aieta, F.; Khorasaninejad, M.; Devlin, R. Recent advances in planar optics: From plasmonic to dielectric metasurfaces. *Optica* **2017**, *4*, 139. [[CrossRef](#)]
12. Yu, N.; Genevet, P.; Kats, M.A.; Aieta, F.; Tetienne, J.-P.; Capasso, F.; Gaburro, Z. Light Propagation with Phase Discontinuities: Generalized Laws of Reflection and Refraction. *Science* **2011**, *334*, 333–337. [[CrossRef](#)] [[PubMed](#)]
13. Shen, X.; Cui, T.J.; Martin-Cano, D.; Garcia-Vidal, F.J. Conformal Surface Plasmons Propagating on Ultrathin and Flexible Films. *Proc. Natl. Acad. Sci. USA* **2013**, *110*, 40–45. [[CrossRef](#)] [[PubMed](#)]
14. Liang, Y.; Lin, H.; Lin, S.; Wu, J.; Li, W.; Meng, F.; Yang, Y.; Huang, X.; Jia, B.; Kivshar, Y. Hybrid Anisotropic Plasmonic Metasurfaces with Multiple Resonances of Focused Light Beams. *Nano Lett.* **2021**, *21*, 8917–8923. [[CrossRef](#)] [[PubMed](#)]
15. Long, Z.; Liang, Y.; Feng, L.; Zhang, H.; Liu, M.; Xu, T. Low-Cost and High Sensitivity Glucose Sandwich Detection Using a Plasmonic Nanodisk Metasurface. *Nanoscale* **2020**, *12*, 10809–10815. [[CrossRef](#)] [[PubMed](#)]
16. Sun, S.; Yang, K.-Y.; Wang, C.-M.; Juan, T.-K.; Chen, W.T.; Liao, C.Y.; He, Q.; Xiao, S.; Kung, W.-T.; Guo, G.-Y.; et al. High-Efficiency Broadband Anomalous Reflection by Gradient Meta-Surfaces. *Nano Lett.* **2012**, *12*, 6223–6229. [[CrossRef](#)]
17. Khorasaninejad, M.; Chen, W.T.; Devlin, R.C.; Oh, J.; Zhu, A.Y.; Capasso, F. Metalenses at visible wavelengths: Diffraction-limited focusing and subwavelength resolution imaging. *Science* **2016**, *352*, 1190–1194. [[CrossRef](#)]
18. Liu, A.Q.; Zhu, W.M.; Tsai, D.P.; Zheludev, N. Micromachined tunable metamaterials: A review. *J. Opt.* **2012**, *14*, 114009. [[CrossRef](#)]
19. Sautter, J.; Staude, I.; Decker, M.; Rusak, E.; Neshev, D.N.; Brener, I.; Kivshar, Y.S. Active Tuning of All-Dielectric Metasurfaces. *ACS Nano* **2015**, *9*, 4308–4315. [[CrossRef](#)]
20. Waters, R.F.; Hobson, P.A.; MacDonald, K.F.; Zheludev, N.I. Optically switchable photonic metasurfaces. *Appl. Phys. Lett.* **2015**, *107*, 917. [[CrossRef](#)]
21. Naik, G.V.; Shalae, V.M.; Boltasseva, A. Alternative Plasmonic Materials: Beyond Gold and Silver. *Adv. Mater.* **2013**, *25*, 3264–3294. [[CrossRef](#)] [[PubMed](#)]
22. Babicheva, V.E.; Boltasseva, A.; Lavrinenko, A. Transparent conducting oxides for electro-optical plasmonic modulators. *Nanophotonics* **2015**, *4*, 436. [[CrossRef](#)]
23. Melikyan, A.; Lindenmann, N.; Walheim, S.; Leufke, P.M.; Ulrich, S.; Ye, J.; Vincze, P.; Hahn, H.; Schimmel, T.; Koos, C.; et al. Surface plasmon polariton absorption modulator. *Opt. Express* **2011**, *19*, 8855–8869. [[CrossRef](#)] [[PubMed](#)]
24. Oleksandr, B.; Nina, P.; Malgosia, K.; Nikolay, I.; Fedotov, V.A. Electrically Controlled Nanostructured Metasurface Loaded with Liquid Crystal: Toward Multifunctional Photonic Switch. *Adv. Opt. Mater.* **2015**, *3*, 674–679.
25. Forouzmmand, A.; Mosallaei, H. All-Dielectric C-Shaped Nanoantennas for Light Manipulation: Tailoring Both Magnetic and Electric Resonances to the Desire. *Adv. Opt. Mater.* **2017**, *5*, 1700147. [[CrossRef](#)]
26. Liu, Z.-Q.; Liu, G.-Q.; Liu, X.-S.; Zhou, H.-Q.; Gu, G. Multispectral Broadband Light Transparency of a Seamless Metal Film Coated with Plasmonic Crystals. *Plasmonics* **2014**, *9*, 615–622. [[CrossRef](#)]
27. Sorger, V.J.; Lanzillotti-Kimura, N.D.; Ma, R.-M.; Zhang, X. Ultra-Compact Silicon Nanophotonic Modulator with Broadband Response. *Nanophotonics* **2012**, *1*, 17–22. [[CrossRef](#)]
28. Park, J.; Kang, J.-H.; Liu, X.; Brongersma, M.L. Electrically Tunable Epsilon-Near-Zero (ENZ) Metafilm Absorbers. *Sci. Rep.* **2015**, *5*, 15754. [[CrossRef](#)]
29. Tahersima, M.H.; Ma, Z.; Gui, Y.; Miscuglio, M.; Sun, S.; Amin, R.; Dalir, H.; Sorger, V.J. Coupling-Controlled Dual ITO Layer Electro-Optic Modulator in Silicon Photonics. *arXiv* **2018**, arXiv:arXiv1812.11458.
30. Amin, R.; Maiti, R.; Carfano, C.; Ma, Z.; Tahersima, M.H.; Lilach, Y.; Ratnayake, D.; Dalir, H.; Sorger, V.J. 0.52 V mm ITO-based Mach-Zehnder modulator in silicon photonics. *APL Photonics* **2018**, *3*, 126104. [[CrossRef](#)]
31. Feigenbaum, E.; Diest, K.; Atwater, H.A. Unity-Order Index Change in Transparent Conducting Oxides at Visible Frequencies. *Nano Lett.* **2010**, *10*, 2111–2116. [[CrossRef](#)] [[PubMed](#)]
32. Tiwari, D.L.; Sivasankaran, K. Nitrogen-doped NDR behavior of double-gate graphene field-effect transistor. *Superlattices Microstruct.* **2019**, *136*, 106308.1–106308.8. [[CrossRef](#)]
33. Schon, J.H. Field-Effect Modulation of the Conductance of Single Molecules. *Science* **2001**, *294*, 2138–2140. [[CrossRef](#)]
34. Cao, Z.; Duan, B.; Yuan, S.; Yang, Y. New super junction LDMOS with surface and bulk electric field modulation by buffered step doping and multi floating buried layers—ScienceDirect. *Superlattices Microstruct.* **2017**, *111*, 221–229. [[CrossRef](#)]
35. Dionne, J.A.; Diest, K.; Sweatlock, L.A.; Atwater, H.A. PlasMOSstor: A Metal-Oxide-Si Field-Effect Plasmonic Modulator. *Nano Lett.* **2009**, *9*, 897–902. [[CrossRef](#)] [[PubMed](#)]
36. Sherrott, M.C.; Hon, P.W.C.; Fountaine, K.T.; Garcia, J.C.; Ponti, S.M.; Brar, V.W.; Sweatlock, L.A.; Atwater, H.A. Experimental Demonstration of >230° Phase Modulation in Gate-Tunable Graphene-Gold Reconfigurable Mid-Infrared Metasurfaces. *Nano Lett.* **2017**, *17*, 3027–3034. [[CrossRef](#)] [[PubMed](#)]
37. Huang, Y.-W.; Lee, H.W.H.; Sokhoyan, R.; Pala, R.A.; Thyagarajan, K.; Han, S.; Tsai, D.P.; Atwater, H.A. Gate-Tunable Conducting Oxide Metasurfaces. *Nano Lett.* **2016**, *16*, 5319. [[CrossRef](#)]
38. Amin, R.; George, J.K.; Sun, S.; de Lima, T.F.; Tait, A.N.; Khurgin, J.B.; Miscuglio, M.; Shastri, B.J.; Prucnal, P.R.; El-Ghazawi, T.; et al. ITO-based Electro-absorption Modulator for Photonic Neural Activation Function. *APL Mater.* **2019**, *7*, 081112. [[CrossRef](#)]
39. Fatemi, R.; Abiri, B.; Khachaturian, A.; Hajimiri, A. High sensitivity active flat optics optical phased array receiver with a two-dimensional aperture. *Opt. Express* **2018**, *26*, 29983. [[CrossRef](#)]

40. Zhewei, W.; Chaonan, C.; Ke, W.; Chong, H.; Ye, H. Transparent Conductive Oxides and Their Applications in Near Infrared Plasmonics. *Phys. Status Solidi (A)* **2019**, *216*, 1700794.
41. Fei, Y.; Shim, E.; Zhu, A.Y.; Zhu, H.; Reed, J.C.; Cubukcu, E. Voltage tuning of plasmonic absorbers by indium tin oxide. *Appl. Phys. Lett.* **2013**, *102*, 1448.
42. Campbell, S.D.; Ziolkowski, R.; Cao, J.; Laref, S.; Muralidharan, K.; Deymier, P. Anisotropic permittivity of ultra-thin crystalline Au films: Impacts on the plasmonic response of metasurfaces. *Appl. Phys. Lett.* **2013**, *103*, 075120. [[CrossRef](#)]
43. Lynch, D.W. Comments on the Optical Constants of Metals and an Introduction to the Data for Several Metals. *Handb. Opt. Constants Solids* **1997**, *1*, 275–367.
44. Vexler, M.I.; Tyaginov, S.E.; Shulekin, A.F.; Grekhov, I.V. Current-voltage characteristics of Al/SiO₂/p-Si MOS tunnel diodes with a spatially nonuniform oxide thickness. *Semiconductors* **2006**, *40*, 1109–1115. [[CrossRef](#)]
45. Li, S.-Q.; Sakoda, K.; Ketterson, J.B.; Chang, R.P.H. Broadband Resonances in ITO Nanorod Arrays. *Eprint Arxiv* **2015**, *63*, 694–698.
46. Siahkal-Mahalle, B.H.; Abedi, K. The Effect of Carrier Distribution on Performance of ENZ-Based Electro-Absorption Modulator. *Plasmonics* **2020**, *15*, 1689–1697. [[CrossRef](#)]
47. Etinger-Geller, Y.; Zoubenko, E.; Baskin, M.; Kornblum, L.; Pokroy, B. Thickness Dependence of the Physical Properties of Atomic-Layer Deposited Al₂O₃. *J. Appl. Phys.* **2019**, *125*, 185302. [[CrossRef](#)]
48. Jin, L.; Chen, Q.; Liu, W.; Song, S. Electro-absorption Modulator with Dual Carrier Accumulation Layers Based on Epsilon-Near-Zero ITO. *Plasmonics* **2016**, *11*, 1087–1092. [[CrossRef](#)]
49. Pshenichnyuk, I.A.; Kosolobov, S.S.; Drachev, V.P. Fine-Tuning of the Electro-Optical Switching Behavior in Indium Tin Oxide. *Phys. Rev. B* **2021**, *103*, 115404. [[CrossRef](#)]
50. Nemati, A.; Wang, Q.; Ang, N.S.S.; Hong, M.H.; Teng, J. Ultra-high extinction-ratio light modulation by electrically tunable metasurface using dual epsilon-near-zero resonances. *Opto-Electron. Adv.* **2021**, *4*, 200088-1–200088-11. [[CrossRef](#)]
51. Horikawa, K.; Nakasuga, Y. Self-heterodyning optical waveguide beam forming and steering network integrated on Lithium Niobate substrate. *Microw. Theory Tech. IEEE Trans.* **1995**, *43*, 2395–2401. [[CrossRef](#)]
52. Ding, K.; Shen, Y.; Ng, J.; Zhou, L. Equivalent-medium theory for metamaterials made by planar electronic materials. *Epl* **2013**, *102*, 28005. [[CrossRef](#)]
53. Zhu, B.; Ren, G.; Zheng, S.; Lin, Z.; Jian, S. Nanoscale dielectric-graphene-dielectric tunable infrared waveguide with ultrahigh refractive indices. *Opt. Express* **2013**, *21*, 17089–17096. [[CrossRef](#)] [[PubMed](#)]
54. Goutzoulis, A.P.; Davies, D.K.; Zomp, J.M. Hybrid electronic fiber optic wavelength-multiplexed system for true time delay steering of phased array antennas. *Opt. Express* **2005**, *31*, 2312–2322. [[CrossRef](#)]